



This is a repository copy of *Battery age monitoring: ultrasonic monitoring of ageing and degradation in lithium-ion batteries*.

White Rose Research Online URL for this paper:
<https://eprints.whiterose.ac.uk/221383/>

Version: Accepted Version

Article:

Williams, D., Green, J., Bugryniec, P. et al. (2 more authors) (2025) Battery age monitoring: ultrasonic monitoring of ageing and degradation in lithium-ion batteries. *Journal of Power Sources*, 631. 236174. ISSN 0378-7753

<https://doi.org/10.1016/j.jpowsour.2025.236174>

© 2025 The Authors. Except as otherwise noted, this author-accepted version of a journal article published in *Journal of Power Sources* is made available via the University of Sheffield Research Publications and Copyright Policy under the terms of the Creative Commons Attribution 4.0 International License (CC-BY 4.0), which permits unrestricted use, distribution and reproduction in any medium, provided the original work is properly cited. To view a copy of this licence, visit <http://creativecommons.org/licenses/by/4.0/>

Reuse

This article is distributed under the terms of the Creative Commons Attribution (CC BY) licence. This licence allows you to distribute, remix, tweak, and build upon the work, even commercially, as long as you credit the authors for the original work. More information and the full terms of the licence here:
<https://creativecommons.org/licenses/>

Takedown

If you consider content in White Rose Research Online to be in breach of UK law, please notify us by emailing eprints@whiterose.ac.uk including the URL of the record and the reason for the withdrawal request.



eprints@whiterose.ac.uk
<https://eprints.whiterose.ac.uk/>

Battery age monitoring: Ultrasonic monitoring of ageing and degradation in lithium-ion batteries

Daniel Williams^a, Joshua Green^a, Peter Bugryniec^b, Solomon Brown^b, Robert Dwyer-Joyce^{a,*}

^a*Leonardo Centre of Tribology, School of Mechanical, Aerospace & Civil Engineering, Engineering Heartspace, Sir Frederick Mappin Building, Mappin Street, S1 3JD, UK*

^b*School of Chemical, Materials & Biological Engineering, The University of Sheffield, Mappin Street, Sheffield, S1 3JD, UK*

Abstract

Lithium-ion batteries, widely used in modern technology, degrade with use, leading to reduced capacity and power output. Monitoring and diagnosing this degradation is essential, and ultrasound has emerged as a potential tool because of its low cost and non-destructive nature. Studies have noted changes in ultrasound behaviour with battery degradation, making it potentially valuable for tracking battery health. However, the behaviour of ultrasound as a battery degrades has been an issue within studies. This paper explores the relationship between state-of-health (SOH) loss and permanent ultrasonic signal changes over 100 charge cycles. A strong correlation was found between SOH reduction, observed to be caused by the loss of lithium inventory (LLI), and shifts in ultrasound signal responses. The analysis of individual peaks within a single acoustic signal showed consistent shifts in time-of-flight (TOF), often trending toward shorter TOFs. In particular, the rate of degradation was not entirely linear, with fluctuations observed across the cycles. These findings suggest that ultrasound can effectively monitor the rate of lithium-ion battery degradation. Future work could expand on these results by inducing varied degradation conditions and cathode chemistries to determine specific TOF shifts, enhancing detection methods for different degradation mechanisms in lithium-ion batteries.

Keywords: Lithium-ion battery; Battery Degradation; Ageing mechanism; Incremental capacity; Ultrasonic acoustics

1. Introduction

1.1. Battery SOC and SOH

Lithium-ion cells have become commonplace in handheld electronics, such as mobile phones and laptops, and in larger energy storage, such as electric vehicles and grid storage since their commercialisation in the 1990s [1–3]. This

*Corresponding author

Email address: r.dwyer-joyce@sheffield.ac.uk, +44 114 222 7736, Professor Robert Dwyer-Joyce
School of Mechanical, Aerospace & Civil Engineering Sir Frederick Mappin Building Mappin Street
Sheffield S1 3JD (Robert Dwyer-Joyce)

can be attributed to their high energy density, high operating voltage, no memory effect, and small levels of self discharge [4, 5]. However, there are limitations with this technology: stress-induced material damage, capacity fade, and thermal instability which can lead to thermal runaway. Optimal use will provide a finite number of charge/discharge cycles, and nonoptimal use will lead to faster degradation of cell life and an increased rate of loss of cell performance [6].

In order to ensure safe, efficient usage of lithium-ion cells, battery management systems (BMS) have been developed and deployed. A BMS can estimate the state-of-charge (SOC) of a lithium ion cell, which is the ratio of the current cell capacity to the maximum capacity of the cell. This can be estimated using measured values, such as Coulomb counting and open circuit voltage lookups, or using modelling approaches such as electrochemical circuit models and neural networks [7, 8]. Other examples of common BMS methods include: the equivalent circuit model, utilising the open-circuit voltage, ohmic internal resistance, and resistor-capacitor network to model a cell [2]; and support vector machines, which use machine learning algorithms to estimate SOC [7]. These approaches each have their individual benefits and drawbacks: experimental methods require less computational effort and allow easier estimations than modelling approaches, whilst having greater estimation errors [9].

BMSs are capable of providing state-of-health (SOH) estimates based on comparisons between current and past cell performance [10], or by measurable parameters and comparisons to electrochemical models [9]. These parameters include, but are not limited to, internal resistance, terminal voltage, and self-discharge resistance [11, 12]. However, all these methods use values that measure the electrical state of the cell and do not provide accurate measurements of the internal physical state of the cell [13]. Hybrid approaches, involving both empirical data and models, can greatly improve SOH accuracy [14], but these require large datasets and greater computing power.

Estimating the SOH of a cell is a complex task. Several definitions and methods are being deployed for SOH estimations. See ref [15] for further details. The SOH can also be estimated as a function of open circuit voltage (OCV), incremental capacity analysis (ICA) curves, [16], and based on the internal resistance of the cell [17]. One of the most common methods to estimate the SOH is by coulomb counting [9]. It is defined as the ratio of the maximum capacity at cycle t , Q_t (A h), to the original maximum capacity, Q_0 :

$$SOH = \frac{Q_t}{Q_0} \cdot 100\% \quad (1)$$

This allows for the capacity fade of the cell to be measured, which can be caused by multiple physical and chemical reactions. These are outlined in the supplementary material in Figure S1.

1.2. Ultrasonic Non-Destructive Monitoring of Lithium-ion Batteries

Recently, there have been many studies using ultrasound to measure internal changes *in-situ* in order to estimate the health and performance of lithium-ion cells [18–22]. Ultrasound is defined as sound with a frequency above the human hearing range, normally around 20 kHz [23]. It is a well-developed non-destructive technique used for detection of surface and subsurface changes in bodies of interest. Piezoelectric transducers are excited to generate ultrasonic pulses that travel through bodies of interest and get partially reflected at interfaces, such as between two materials, a crack or an air bubble. In addition to monitoring, ultrasound has been used to improve the leaching of active materials from spent LIBs [24, 25] which exposes the cells to high powered, continuous wave. The improvement in the electrochemical performance of LIBs via ultrasound has also been investigated by subjecting cells to a continuous low power acoustic energy [26].

The relationship between ultrasonic signals and battery SOH is complicated when considering the numerous side reactions that can affect the SOH. Side reactions occur almost everywhere because of the electrochemical nature of LIBs, both during normal and abusive conditions. Such reactions include lithium plating, SEI formation and growth, gassing, electrode delamination, and porosity [27, 28]. Post-mortem analysis has confirmed these reactions to be detected, however there is an issue of decoupling these effects for more accurate detection. If multiple reactions occurred within a cell, the ultrasonic response would not be able to discriminate between them.

When LIBs are cycled, there is a cyclical, reversible change in the TOF through the cell that correlates with the SOC. As the cell is charged, the TOF decreases; as the cell is discharged, the TOF increases. There are different reports on the direction of the permanent TOF shift in the literature. The TOF also experiences a non-reversible shift as the cell degrades, which is independent of the SOC. This overall TOF shift is related to the SOH (distinct from the cyclical TOF change driven by the SOC) and is hereafter called the permanent shift. The permanent shift has been observed with different acoustic frequencies, from 90 kHz to 2.25 MHz. The direction of the permanent shift varies within the literature; a permanent shift to a shorter TOF was observed by [22, 29], while a longer permanent shift was observed by [19, 20, 30].

Using a low C-rate reduces the self-heating temperature of the cell due to ohmic heating (heat from the resistance of lithium-ions moving through the electrolyte) and allows for even lithium-ion deposition dispersion [31]. This allows for a more isolated look at degradation methods caused by chemical physical reactions as a result of normal operation rather than as a result of extreme external factors. As stated in [32], some degradation methods occur outside the safe operating conditions, such as cathode degradation at relatively high temperatures (45 °C) [33] and electrode damage and potential rupture at high C-rates [34].

In this work, temporally resolved ultrasonic TOF measurements are performed in lithium-ion cells to investigate

the effect of cell degradation on the permanent shift of the acoustic signal. The cells were cycled for over 100 cycles at a low C-rate within the manufacturer's voltage limit to mitigate pronounced degradation whilst ageing. The cycle number was selected as the cells were rated for 301 cycles by the manufacturer, so the effect of cell ageing is accelerated. This allows for a comparative exploration into ageing and the effects on the ultrasonic response. Multiple reflections were analysed to investigate and compare correlations and permanent shift directions between peaks with different TOF within the A-Scan.

2. Experimental

2.1. Battery Instrumentation

This work involved testing two nominally identical cells, cell A and cell B. The cells were commercial pouch lithium-ion batteries 2000 mA h with consisted of a cathode with NMC chemistry and a graphite anode (stock number 125-1266 RS Pro, London, England) with dimensions of 63 x 43.5 x 7 mm. The cells were purchased at the same time, from the same manufacturing batch and were manufactured on the same day. The cells were instrumented with a single ultrasonic piezoelectric transducer of dimensions 10 mm x 5 mm with a central frequency of 2 MHz. (DeL Piezo Specialties, LLC, FL, US), which were bonded to the cell surface using a commercial adhesive. The centre frequency influences the penetration depth, signal attenuation and wave sensitivity. Based on previous studies [5, 35, 36], 2 MHz was determined as the most suitable frequency. Each cell was instrumented with a single transducer that would act as both transmitter and receiver. A thermocouple was attached to the surface of each cell to record the surface temperature.

2.2. Ultrasonic Pulsing and Receiving

The acoustic response was obtained using a Picoscope 5444D oscilloscope, operated by proprietary Picoscope 6 software (Pico Technology, Cambridgeshire, UK). The Picoscope acted as both a function generator and an acoustic DAQ. The signal was produced by, and the reflections were captured by the Picoscope.

The acoustic signal was controlled through a bespoke virtual instrument (VI) built in LabVIEW, utilising the Picoscope 6 software. This VI also allowed recording of the surface temperature along with the ultrasonic signal, both of which were recorded once a minute. Each capture lasted for one second and recorded 50 pulses, of which the average was taken and used for analysis. The resolution of each pulse was 3900 discrete measurements. This provided a sampling interval of 7.7 ns over a time window of 30 μ s. The source wave for each pulse consisted of three sinusoidal waves, with an amplitude of ± 2 V, that transmitted through the cell and were reflected back to the transducer once they reached the opposing face of the cell. The surface temperature of the cells was monitored using a K-type thermocouple. The temperature was recorded using the NI-9211 temperature input module (National

Instruments, TX, US).

Both cells were cycled at the same time. To capture the acoustic data from both cells, a bespoke multiplexer was used to connect the cells to the Picoscope. This allowed a single Picoscope channel to be used. A sequence table was created to control the acoustic inputs and the parameters of the recorded response. As the cells were connected through a single channel, cells were recorded sequentially. The VI was also designed to receive multiple thermocouple inputs at the same time.

2.3. Battery Cycling

The cells had a maximum charge rate of 0.5 C and a maximum discharge rate of 1 C and were cycled at 600 mA h (0.3 C) using a MACCOR Model 4600A Automated Test System (MACCOR, OK, US) in a constant current-constant voltage (CC-CV) cycle. Internal heat generation has been shown to have a dependency on the C-rate, with higher C-rates resulting in greater heat generation [37]. An increase in heating can cause accelerated ageing in LIBs [38]. The focus of this work is to investigate degradation through internal mechanical and structural changes with reduced influences from controllable factors such as C-rate and temperature. Ultrasonic equipment can be sensitive to temperature, and the exploitation of this is called ultrasound thermometry [39]. To reduce the influence of temperature on the ultrasonic response to ensure that cell ageing has the greatest influence, the C-rate for this work was kept low. The charge cycle saw the cells charged between 3.0 V (0% SOC) and 4.2 V (100% SOC). The upper and lower voltages were held constant until the current dropped below 60 mA h (0.03C) (see Table 1).

Phase	Mode	Voltage (V)	Current (mA)
Charge	Current current	3.0 to 4.2	600
	Constant voltage	4.2	600 to 60
Discharge	Constant current	4.2 to 3.0	600
	Constant voltage	3.0	600 to 60

Table 1: Charge cycle parameters.

2.4. Signal Processing

The charge data, surface temperature, and acoustic response were recorded every 60 seconds throughout the test. The reflected signal (A-Scan) of cell A at the beginning of the test is shown in Figure 1a. The acoustic signal contained information such as the TOF and the signal amplitude. The charge data includes information on the voltage, current and estimated battery capacity. To correlate the acoustic data with the charge and temperature data, a method called peak tracking was employed. In Figure 1a, the first seven peaks are related to the pulse generated that created the acoustic signal and the associated damping. These peaks are highlighted by the blue shading. The other peaks relate to reflections or reflected signals - acoustic signals that have travelled through the cell and returned to the transducer.

As lithium ion cells have multiple layers, either rolled or layered, there are many interfaces. The cells used in this work were purchased from the same batch at the same time. Due to the nature of cell manufacturing, there may be differences between the cells.

Each interaction between the acoustic signal and an interface results in a part of the signal being reflected in the original medium and a part transmitted in the new medium. Therefore, some signals can get trapped reflecting between two interfaces, whilst some of the signal travels through the entirety of the cell. The signal detected by the transducer is a superposition of all the reflections that have split within the cell. A single interface cannot be related to a single peak as a result of this, as the number of interfaces that are superimposed in the signal increased as the TOF increased. Therefore, the highest peak is unlikely to have the best correlation, as investigated by [5]. In order to ensure that the peaks analysed provide the strongest correlation to the loss in SOH, a peak tracking method was employed.

Peak tracking involved selecting individual peaks and recording the respective TOF and amplitude change throughout the cycles [5]. This is done by creating windows centred on the peaks representing a set distance either side of the selected peak in the TOF domain. Between each data point, the greatest amplitude is found within the window range is found, and the windows were shifted to maintain the original set distance from the new peak. This is repeated throughout the dataset, resulting in a spectrogram of the A-Scan focused on the peak in question. This method allowed for the identification of the peak that had the strongest correlation with the internal battery changes.

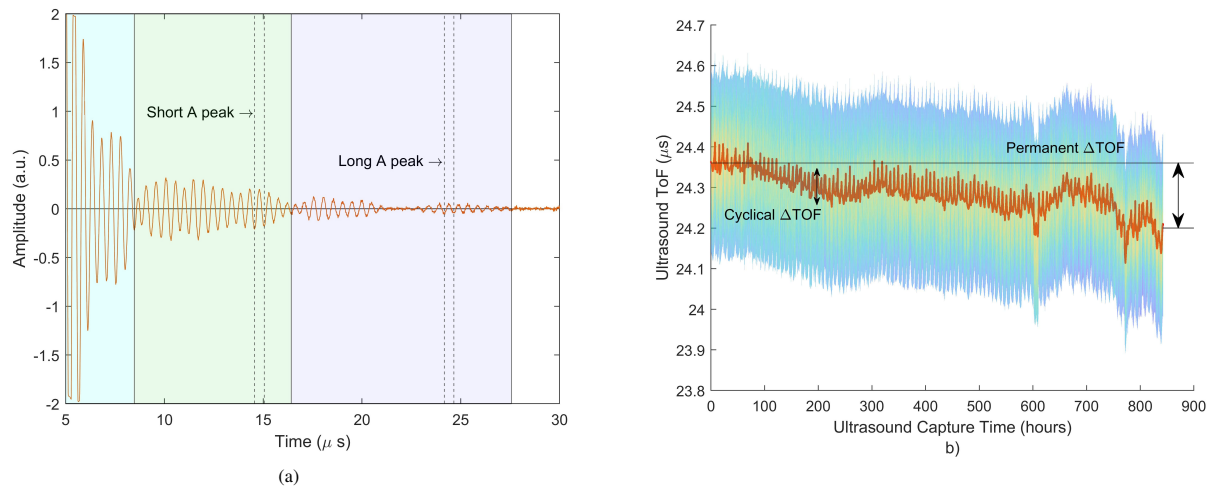


Figure 1: a) A-Scan of Cell A, with the window around peaks Short A and Long A shown with dashed lines. The green and blue shaded areas highlight the first full and second full reflections, respectively. b) TOF of peak Long A using peak tracking. The colour of b) represents to amplitude of the peak capture area, shown in the colourbar. The red lines in b) highlights the peak in the range; the greatest value within the peak capture area.

Selecting multiple peaks individually creates the capability to compare the results of individual peaks across the

A-Scan. In doing so, two peaks were selected for each cell. For cells A and B, these are Short A, Long A, Short B, and Long B, respectively. The naming convention is related to where in the A-Scan (i.e. the TOF) the peaks were selected. Short A and Short B were selected from earlier peaks in the A-Scan, and Long A and Long B were selected from later peaks. The reason for this is due to the internal structure of the cells tested. The cells have a prismatic winding construction which results in spacing in the centre of the cell. This spacing is enough to create an acoustic barrier and was confirmed by Copley et al. when a genetic algorithm was able to accurately predict the internal construction of the cell [40]. The algorithm identified an irregularity in the centre of the cell, which corresponds to a prismatic winding construction. This spacing resulted in a proportion of the signal being reflected. The resultant reflected signal is a half-reflection in which the signal has only travelled back and forth through half the cell. As such, the second reflection was a superposition of the half-reflection after two passes, and the full reflection having made one pass.

Figure 1a shows the A-Scan of cell A. The two peaks, Short A and Long A, are highlighted with the dotted lines. The green shaded area identifies the first two reflections, or the first half-reflection and first full reflection, as described earlier. The blue shaded area therefore emphasises the third and fourth reflections. The change in the TOF of peak Long A, highlighted in Figure 1a, over all the charge cycles is shown in Figure 1b. The colour of the plots change from yellow to blue as the signal amplitude decreases. The red line denotes the location of the peak that is being tracked within the peak window of Long A. In order to improve the signal-to-noise ratio of the signal, the selected peaks were denoised using wavelets via the `wdenoise` function in MATLAB.

What can be seen in Figure 1b is a cyclical increase and decrease in ToF alongside a general trend to a shorter TOF. The cyclical change is related to the charging cycle of the cell, as lithium-ions intercalate and deintercalate into and out of the electrodes. This TOF variation is therefore related to the SOC of the cell. The general trend to a shorter TOF (or the permanent decrease in TOF) is related to the loss in SOH of the cell. This relates to non-reversible changes in the cell such as LLI or LAM. The kink seen around 600 hours into the test will be discussed in the next section.

Tracking single peaks allows for direct comparison between the battery, temperature, and acoustic data. Figure 2 shows this comparison for four charge cycles for cell A, using the same peak in Figure 1. There is a clear correlation between the acoustic and battery data, as the TOF (Figure 2e) shows a decrease as the capacity (Figure 2a) increases, whilst the inverse is true for the amplitude (Figure 2d). The temperature is shown to exhibit cyclical behaviour, as the temperature increases significantly as the cell nears the end of the discharge stage, followed by a sharp decrease as charging begins.

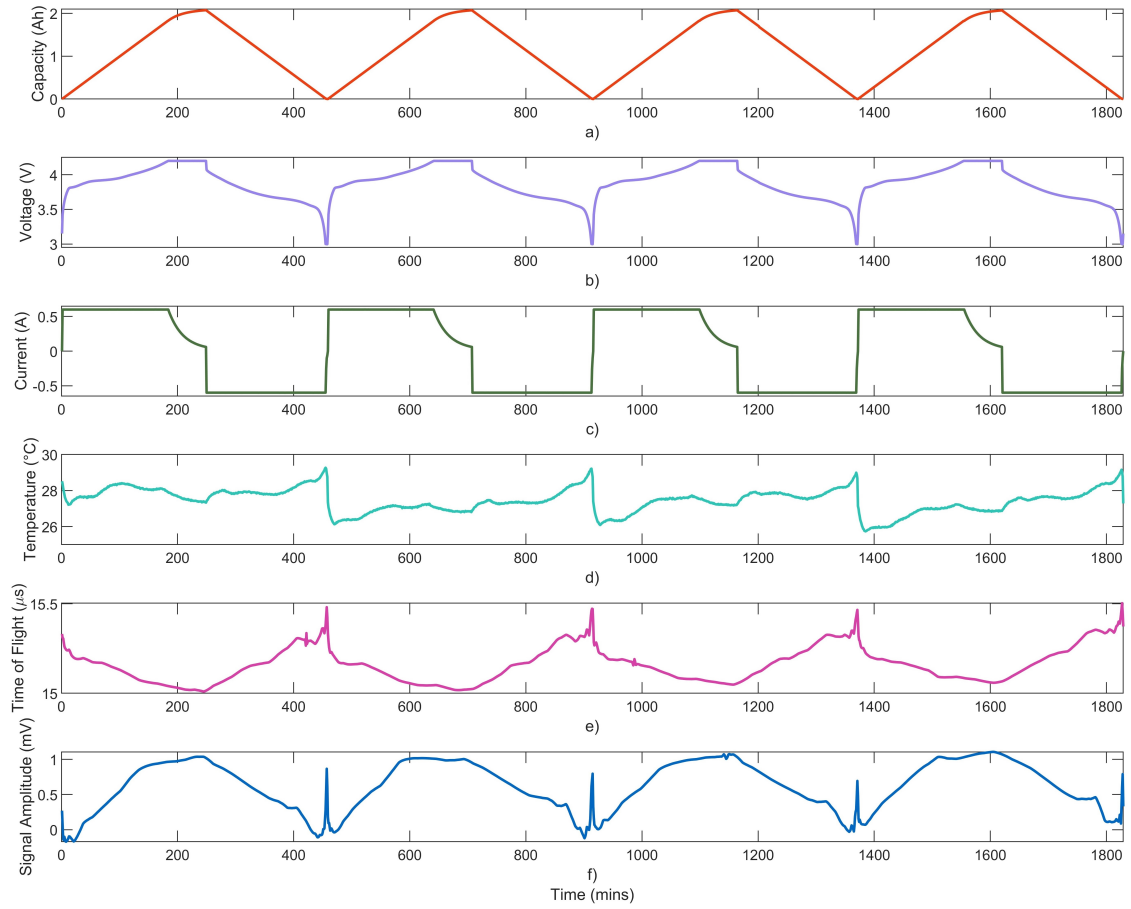


Figure 2: Change in a) capacity, b) voltage, c) current, d) temperature, e) time-of-flight over four cycles and f) signal amplitude. The amplitude and time-of-flight are from peak Short A. A cyclical response from the acoustic signal and the temperature can be seen that correlates with the charge cycles of the cell.

3. Results and Discussion

3.1. Generated ultrasonic signal generated by a pouch cell

The amplitude of the reflected wave as it varies with time (known as an A-Scan) is recorded. Figure 3 shows an A-Scan response from one of the lithium-ion cells used in this work. The 2Ah cells used in this work are the same cells used by Copley et. al, which were described to contain around 15 "unit cells", each containing multiple interfaces [40]. The authors described a "unit cell" as a repeating pattern of battery components consisting of two anode layers, two cathode layers, two current collectors, an electrolyte, and two separators. Each interface acts as an acoustic reflector, and the resultant A-Scan is a superposition of all internal interfaces within the body. For this reason, the peaks seen in Figure 1 do not correspond to individual layers or structures within the cell, but rather to a superposition of many layers and structures. The speed a longitudinal ultrasonic pulse travels through a medium, c (m s^{-1}), is defined by:

$$c = \sqrt{\frac{E}{\rho}} \quad (2)$$

where E (MPa) is the elastic modulus of the material and ρ (kg m^{-3}) is the material density. As lithium-ion cells charge and discharge, the material properties of the electrode change based on the amount of lithium (de)intercalated within. This influences how the ultrasonic signal travels through the cell, resulting in the difference seen in Figure 3. The A-Scan can vary in two ways: the time-of-flight (TOF) and amplitude. The TOF is the time it takes for an ultrasonic signal to travel through a medium and be received by a transducer, and for a homogeneous material, with known speed and thickness, is calculated using the relationship between c , distance d and time t :

$$c = \frac{d}{t} \quad (3)$$

The use of a pulse-echo setup in this work means the distance travelled by the reflected signal is $2d$, as it must make a round trip to and from the transducer. The TOF in this work was measured using the electrical signal generated by the excitation of the transducer once the reflected wave returned. A cell is not a homogeneous material, with different materials for the electrodes, current collectors, separator and electrolyte, the travel time of the wave will fluctuate with changes in the speed of sound described in Equation 2.

The signal amplitude is the intensity of the acoustic wave. The signal attenuates as it travels through a medium, due to a combination of scattering and absorption. This attenuation results in the decay of the signal amplitude. Scattering is the result of heterogeneity in a material. This could be caused by flaws within a single host medium, or the sudden change in acoustic impedances found at medium interfaces. Absorption is the conversion of acoustic energy into heat by the host medium. When only accounting for these factors, an exponential function can be used to describe the attenuation of an acoustic signal:

$$A = A_0 e^{-\alpha d} \quad (4)$$

where A_0 and A are the initial and final acoustic amplitudes, respectively, α is the attenuation coefficient and d is the distance travelled by the wave. As seen in Figure 3b, the A-Scan shows that the time-of-flight (TOF) increases as the SOC drops, that is, the peaks shift to the right of the A-Scan. The amplitude of some peaks show an increase, while some show a decrease in amplitude with a change in SOC.

The reflection at an interface is described by the reflection coefficient R , which is the ratio of the reflected wave back divided by the incident wave. The reflection coefficient depends on the acoustic impedances of the two media, and is determined by:

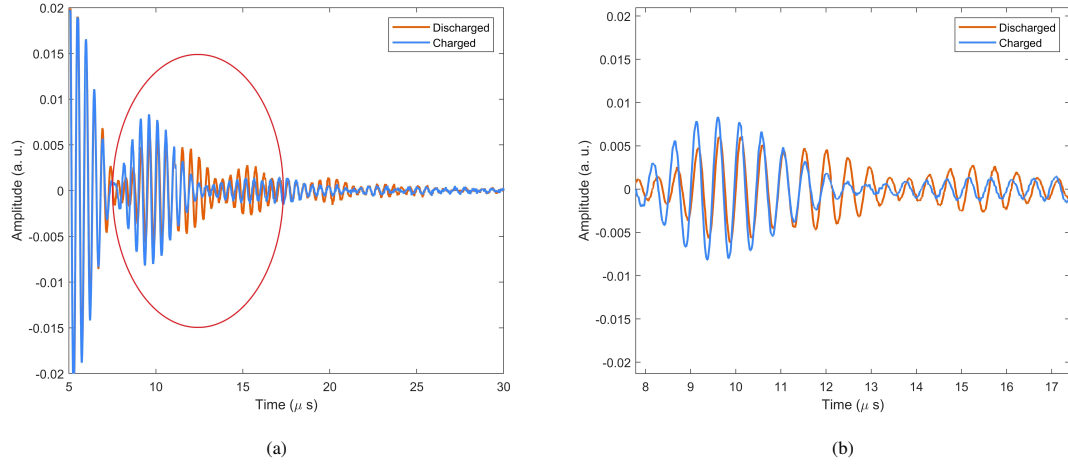


Figure 3: a) An A-Scan of one of the tested cells at full charge (blue) and full discharge (orange). The A-Scan section in the red circle is shown in b) to isolate the first two reflections.

$$R = \frac{Z_2 - Z_1}{Z_2 + Z_1} \quad (5)$$

where Z (Pa s m^{-1}) is defined by:

$$Z = \rho c \quad (6)$$

3.2. Cell degradation

The SOH of both cells, obtained using Equation 1, is shown in Figure 4. It should be noted that the decline is not perfectly linear, as there are SOH fluctuations present in both cells. Batteries such as lithium-ion can suffer from self-charging when certain conditions are met, causing a sudden, temporary increase in available capacity in the next cycle. This is known as regeneration phenomena, which can affect the accuracy and precision of SOH estimations [41–43]. The significance of fluctuations due to regeneration phenomena on the ultrasonic response will be explored in Section 3.4. Cell B underwent more significant fluctuations than cell A, with a significant drop around 20 cycles. Both cells were tested in tandem using the same protocol as described in Table 1, reducing the probability of environmental influences on the cells. Variation in cell performance and degradation behaviours is a well-known problem when it comes to manufacturing [44]. These variations can be attributed to three main factors: the amount of active material (anode and cathode) present in the cell; the resistance to the flow of Li-ions (polarisation resistance); and localised kinetic factors (intercalation) [45]. Given the low C-rate of the charge cycle, the localised kinetic factors will play a less significant role in the variation seen between the two cells. As the cells are from the same batch, the difference in

polarisation resistance is the likely explanation for this difference in degradation behaviours.

Figure 4 also shows the change in temperature of cells A and B during the test. The dotted lines represent the temperature at which the cells were fully discharged, and the solid lines represent the fully charged temperature. The fluctuations at the start of the cycle for cell B, and the drop at cycle 81 in cell A, can be seen to replicate in the temperature readings. The temperature trends outside these isolated points follow the non-linearity of the loss in SOH, but not to the same extent. This is because internal heat generation depends on the final capacity of the cell. A cell that is closer to fully charged or fully discharged will generate more heat [46].

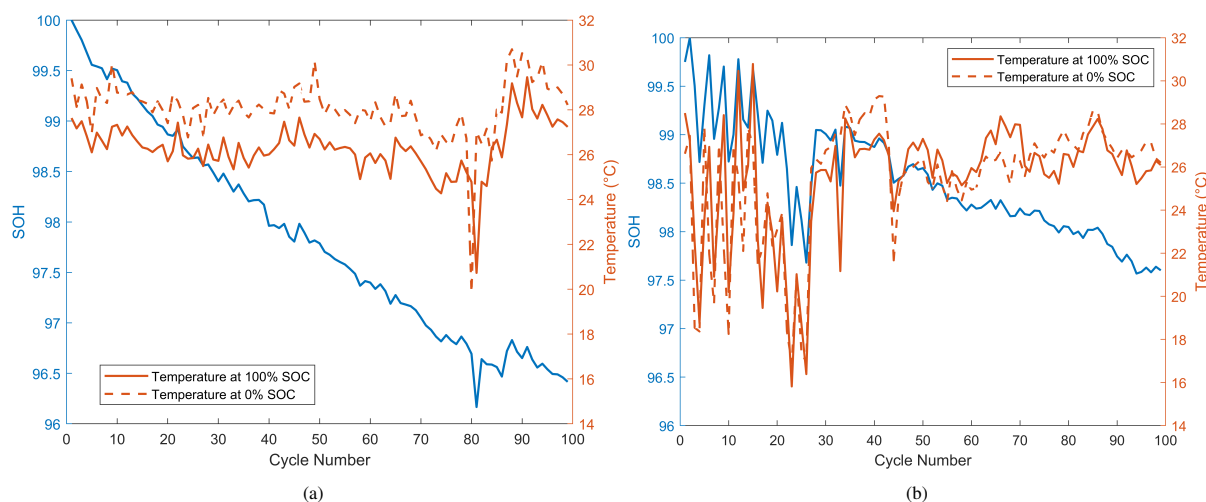


Figure 4: Change in temperature of a) cell A and b) cell B at 0% SOC (dotted line) and 100% SOC (solid line) against the SOH drop.

Aside from these fluctuations, the temperature of the cells does not show a permanent trend that matches the SOH drop - the temperature range remains consistently within 24 - 30 °C for both cells. The regeneration phenomenon is reflected in the temperature, as fluctuations are seen in both fully charged and fully discharged temperature readings. As the testing was not performed in a temperature controlled environment, variations are also a result of slight room temperature changes. In a semi-empirical degradation model by [47], the main mechanism of battery degradation in a cell between 25 - 30 °C is the SEI layer growth. This growth is caused by an interaction between the electrolyte and active lithium-ions, leading to the formation of a surface layer film on the anode. This process consumes lithium ions, reducing the effective capacity of the cell over time [48, 49], while increasing internal resistance [50].

In order to understand which driving forces are causing the cell degradation, incremental capacity analysis (ICA) curves of the cells were employed. This analysis involves the differentiation of the capacity with respect to the voltage, allowing voltage plateaus to be highlighted as peaks, as defined in Equation 7.

$$\frac{dQ}{dV} = \frac{Q_t - Q_{t-1}}{V_t - V_{t-1}} \quad (7)$$

$$Q_t = \int_0^t I dt \quad (8)$$

where Q_t and V_t are the capacity and voltage at time t , and I is the current. Changes in these peaks were evaluated as the number of cycles increased. Through these equations, plateaus in the voltage curve are converted into peaks in the ICA plot [51]. A rolling average with a window of 5 steps was applied to smooth the ICA curves. Figure 5 shows the ICA plots of the two cells tested. Two peaks corresponding to voltage plateaus were observed. These peaks seen during charging relate to graphite intercalation and the crystal structure change of the cathode, respectively [52]. As such, the peaks are strongly dependent on the cell chemistry [53].

For charge (Figure 5a and 5c) and discharge (Figure 5b and 5d) for both cells, the ICA peaks trend to a higher voltage as the cells are cycled i.e. the peaks shifted to the right. According to [54], this shift can be used to ascribe the main driving mechanism for the capacity drop as LLI as seen in Figure 5e. The increase in voltage is due to the incomplete lithiation of the anode as an increasing number of lithium ions are consumed by parasitic reactions, such as the SEI growth. The voltage limits were kept the same (3.0 - 4.2 V) throughout the tests.

As the SEI grows, more lithium ions are consumed, which has the effect of reducing the lower potential regions of the anode. This results in incomplete lithiation during charging, resulting in a higher potential at the end of charge. To maintain the upper voltage limit, the cathode would have to compensate for a higher potential. The same is then true for the discharge, as the cathode would experience incomplete lithiation at the end of discharge to maintain the lower voltage limit [55]. The amplitude of the ICA curve peaks also consistently decreases as the cell ages, further indicating that the lithiation of the electrodes is reduced due to LLI [56].

This degradation phenomenon agrees with the literature on cell degradation methods of NMC / graphite cells (see Figure 5e) [57–59]. LLI has been found to be the most prominent degradation mechanism at the anode [60]. The main cause of LLI has been found to be SEI formation and growth on the anode [61].

3.3. Ultrasonic response changes during degradation

The relationship between the SOH and the ultrasonic response was investigated, using the methods described in Section 2.4. In this case, the Spearman correlation coefficient was employed to determine the correlation of SOH estimation with the ultrasonic signal parameter throughout the test. The Spearman correlation coefficient r_s can be computed using:

$$r_s = \frac{cov(x_i, y_i)}{\sigma x_i, \sigma y_i} \quad (9)$$

where $cov(x_i, y_i)$ is the covariance of the rank variables x_i and y_i for the original data and $\sigma x_i, \sigma y_i$ are the standard

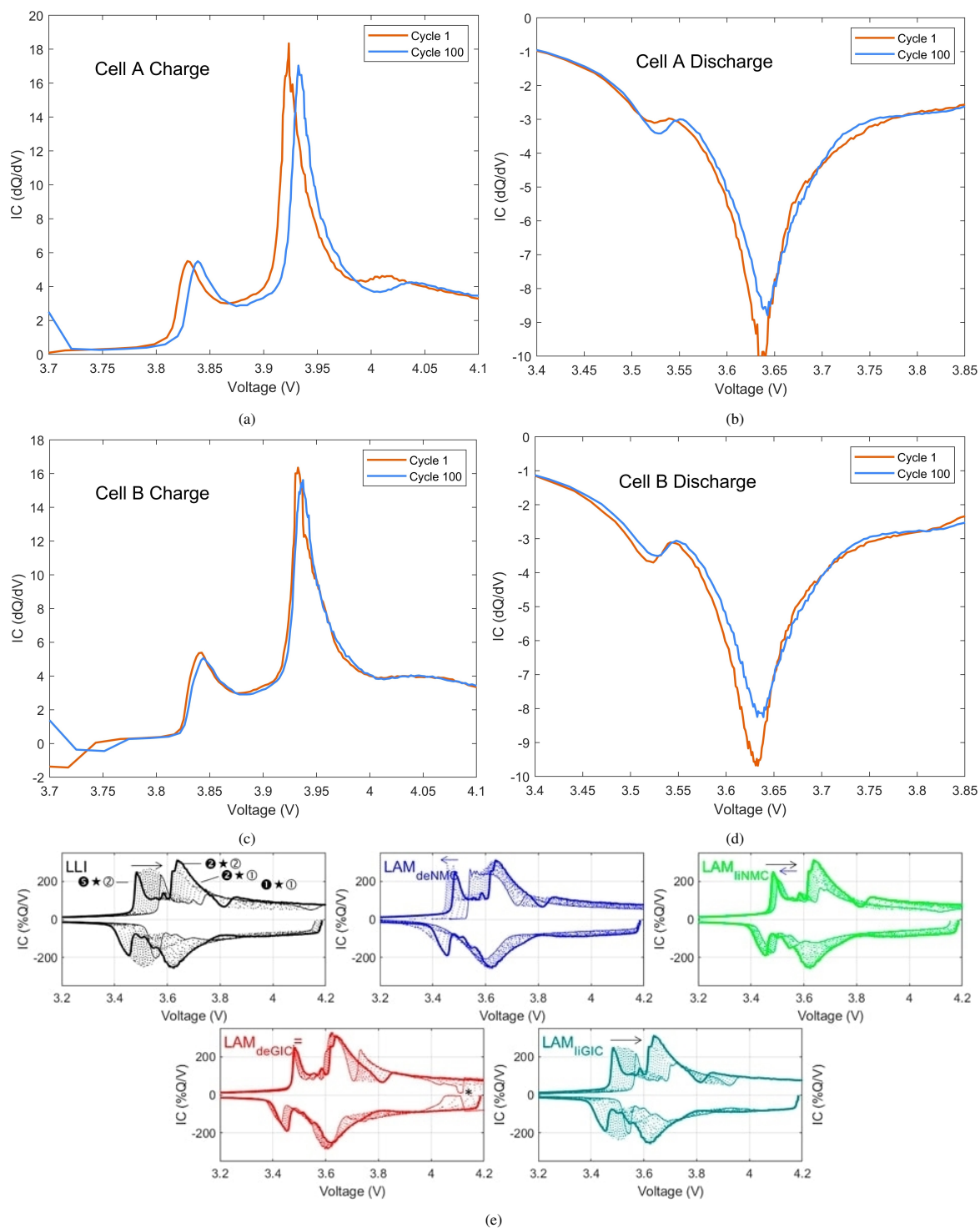


Figure 5: The ICA of cell A during a) charge and b) discharge. The ICA of cell B is represented in c) and d). All plots show a trend to a higher voltage as the cell ages. e) shows how the ICA of an NMC/graphite cell would change when influenced by different degradation methods. deNMC = delithiated cathode; liNMC = lithiated cathode; deGIC = delithiated anode; liGIC = lithiated anode. Image adapted from [54], licensed under CC BY 4.0. Modifications were made to only include graphs related to LLI and LAM changes.

variations of the rank variables. The r_s ranges from -1 to +1, where -1 is a perfect monotonous decreasing correlation and +1 is a perfectly monotonously increasing correlation. This was determined to best evaluate the relationship between the SOH and TOF as the change in TOF was observed to not be consistently linear. Similar statistical models, such as the Pearson correlation, would therefore not be best suited, as this would prioritise the linearity of the relationship.

The Spearman correlation coefficient was calculated for the TOF of all peaks in the A-Scan (for example, all peaks seen in Figure 1a against the change in SOH. Cell A saw 41 peaks were compared and cell B saw 40 peaks compared. From that, using the definition of Short and Long reflections in Section 2.4, four peaks were found with two peaks for cell A and two for cell B. For Short A and Long A, the coefficient was -0.831 and 0.821, respectively. For Short and Long B, the coefficient was 0.906 and 0.810, respectively. All absolute values were above 0.8, which indicates a strong correlation between the permanent TOF shift and capacity fade. Notably, the short TOF for both cells had greater absolute values than the long TOF, which suggests that shorter TOF - signals that are reflected back earlier through the cell - are more reliable at detecting capacity fade. This could be related to the reduced number of superimposed interfaces on the signal, as the signal would have travelled through half of the cell rather than through the whole cell. This would require the assumption that the ratio of lithium-ions between the electrodes is consistent throughout the whole cell. It should be stated that not all peaks are equal; there were some peaks that had Spearman correlation coefficients nearing 0, suggesting a lack of correlation between the TOF and capacity fade. This highlights the importance of ensuring that the correct peak is used, not just the largest peak, when estimating the SOH of a cell. Correct meaning the the peak with the strongest correlation between TOF and SOH.

The changes in acoustic signal against the change in SOH are shown in Figure 6 (where Figure 6a and 6c are Short A and Short B, and 6b and 6d are Long A and Long B, respectively). The colour gradient is employed to signify the cycle number, wherein the gradient transitions from a lighter hue (earlier cycles) to a darker one (later cycles). The ultrasonic response for all cells showed deviation from cycle 1, which is considered the baseline signal. The average capacity fade for cell A was approximately 0.03% per cycle, and cell B had an average capacity fade of 0.02% per cycle. After 100 cycles, cell A had a remaining capacity of 96.42% and cell B had 97.6%.

Short A saw an increasing TOF change of 0.876 μs alongside a capacity fade of 3.58%. Conversely, Short B saw a decreasing TOF of 0.0393 μs over a 2.15% capacity drop. Long A saw a decrease in TOF by 0.101 μs over a drop in capacity of 3.58%. And Long B saw a permanent negative change in TOF for the long TOF of 0.109 μs over a drop in capacity of 2.15%. This is summarised in Table 2.

All peaks except Short A saw a linear decrease in TOF, which saw a significant increase. There are several potential reasons that can result in unpredictable and unstable acoustic results [62]. One of these reasons is cell-to-cell

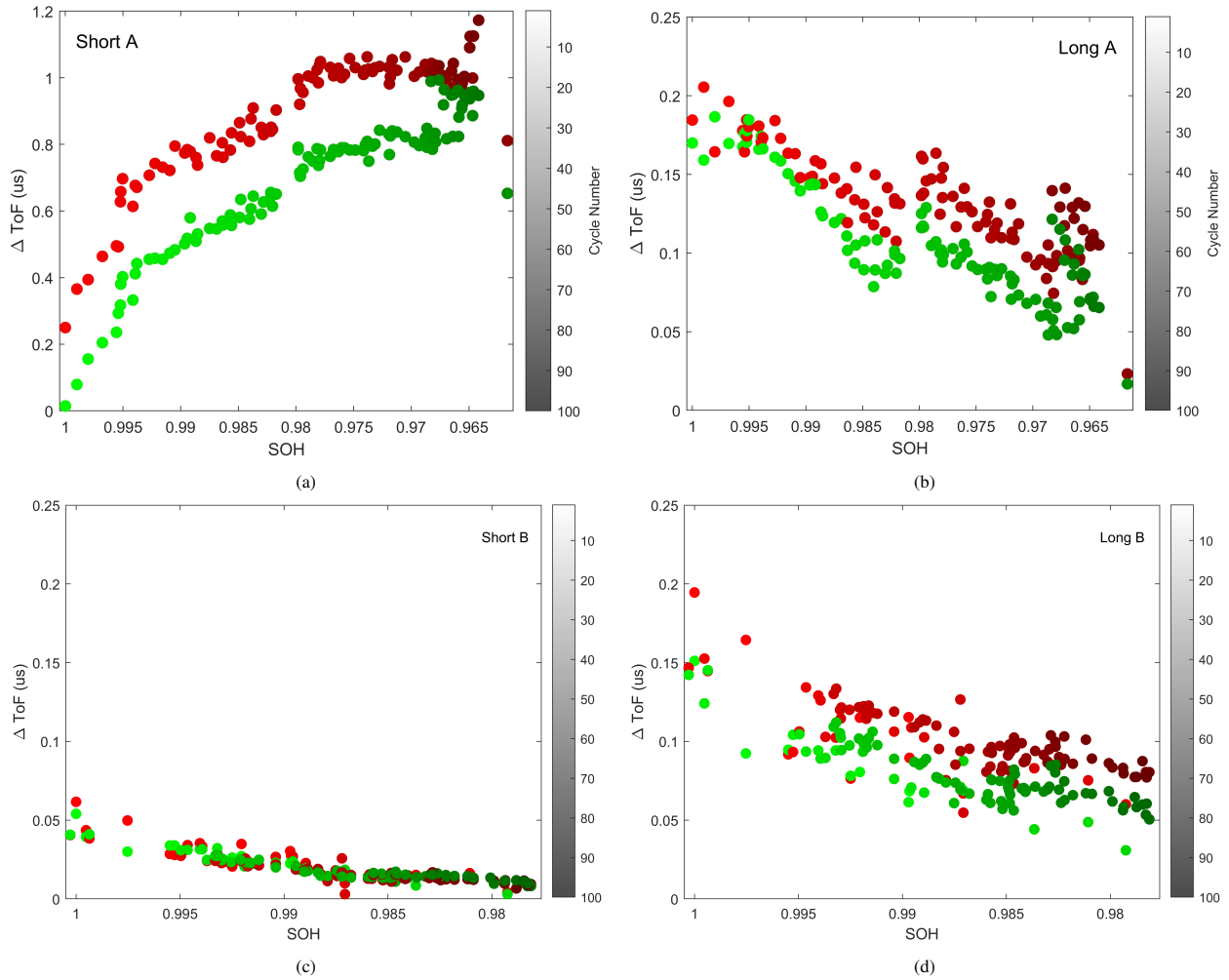


Figure 6: Comparison of (a) Short A, (b) Long A, (c) Short B and (d) Long B over 100 cycles. The green dots represent a SOC of 100% and the red dots represent a SOC of 0%. The hue of the dots represents the cycle number: the hue darkens as the cycle number increases. It should be noted the y-axis for a) is much larger than for the other figures to allow for readability.

manufacturing variation. There is limited coordinated effort to quantify such variations in product specification. This can result in variations not being identified until after experimental studies on the complete cell [63]. Another possible source of the difference observed between nominally identical cells The other is the transducer and associated bonding method. As the transducer is extremely sensitive, any difference in the surface it is bonded to, the pressure applied to the transducer, the frequency, the type of couplant and the quality of the probe can have significant effects on the signal [64]. In this case, the transducers were from the same manufacturing batch, used the same couplant and were bonded using the same method, reducing the signal variation due to the transducer and bonding.

As the maximum capacity is decreasing with each cycle, the TOF difference between fully charged and fully discharged should see some slight changes as a result of the decreased Li-ion movement. Both cells produced results

that differed from one another. Short A started with a difference of $\tilde{0}.24 \mu\text{s}$, which decreased linearly to $\tilde{0}.17 \mu\text{s}$. For the later peak, Long A started at $0.02 \mu\text{s}$, ended at $0.04 \mu\text{s}$. Both the selected peaks in cell B did not exhibit changes in the TOF difference as the cell degraded. Short B had a consistent average of $\tilde{0}.0052 \mu\text{s}$, and Long B was constant at $\tilde{0}.024 \mu\text{s}$. Both peaks saw very similar differences for each cycle, only differing in magnitude. The drop in SOH seen in Figure 4b and the difference in TOF seen in Figures 6b and 6c align well, suggesting accurate acoustic measurements of the maximum cyclical capacity of the cell.

As can be observed, there is an apparent consistent change in the TOF implying that the internal changes within the cell were being detected. Given the rate of degradation is seen to be relatively linear in Figure 4, linear regression was utilised to determine the TOF shift matched the capacity fade. Regression was used to determine the relationship of the TOF and the SOH by fitting a linear equation to the data, shown in Figure 7. This provided an R-squared (R^2) that ranges between 0 and 1, where 0 means no correlation between the SOH and TOF and 1 is a perfect correlation between the two variables.

Figure 7 shows the R^2 values for the selected peaks of both cells and is summarised in Table 2. The short TOF had a greater R^2 for both cells, further suggesting that shorter TOF measurements have a stronger relationship with SOH regardless of the shift the signal undergoes. The degradation rate has been found to depend on the cathode chemistries and operating conditions [65]. For NMC cells, the rate degradation rate decreases as the cell is cycled long term [66]. As seen in Figures 6a and 6c, there is a slight gradient change as the SOH drops, which is not as visible in the Long reflections. Longer term testing would be needed to confirm this SOH bias to the Short reflections.

Cell	Capacity Drop (%)	Capacity Drop per Cycle (%)	Peak	Spearman Correlation Coefficient	TOF Change (μs)	TOF Shift / Capacity Drop ($\mu\text{s} / \%$)	Linear Regression
A	3.58	0.03	Short A	-0.831	0.876	0.245	0.874
			Long A	0.821	-0.101	-0.028	0.756
B	2.4	0.02	Short B	0.906	-0.0393	-0.018	0.898
			Long B	0.81	-0.109	-0.051	0.753

Table 2: Summary of capacity and TOF changes, along with correlations, for both cells and selected peaks.

A shift to a shorter permanent TOF means a faster speed of sound through a cell. Using Equation 2, it can be assumed that this is in part caused by an increase in E (MPa), a decrease in ρ or a combination of the two. Conversely, a permanent shift to a larger nominal value would suggest the difference is decreasing. This is demonstrated within a single cycle, where the lithium-ions intercalate and de-intercalate with the anode and cathode. During charge, the lithium-ions de-intercalates from the cathode and intercalates into the anode, and the reverse is true when discharging.

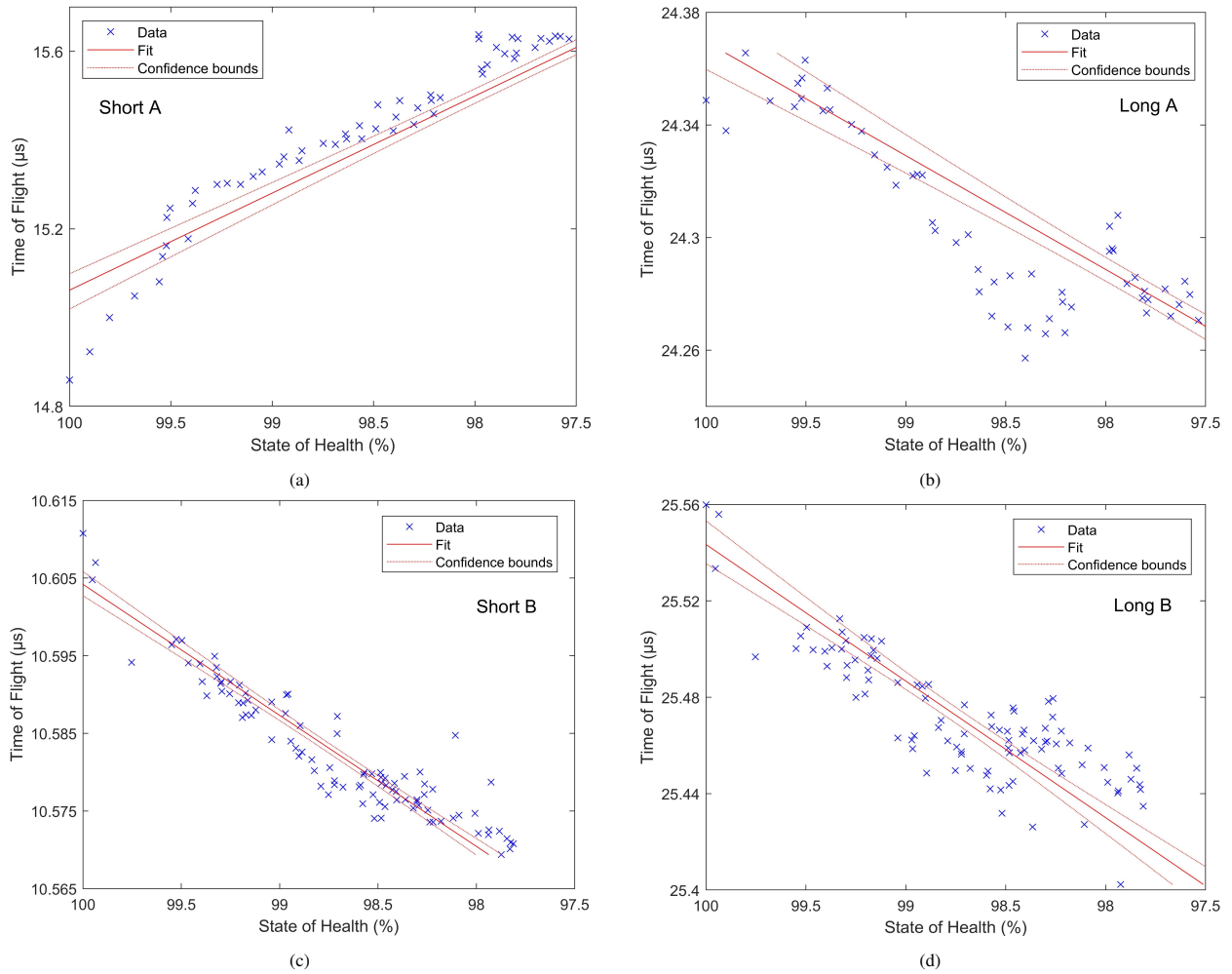


Figure 7: R^2 plots for a) Short A, b) Long A, c) Short B and d) Long B. The shorter peaks showed a stronger correlation with SOH compared to their longer counterparts.

It has been shown that the anode has a much greater sensitivity to changes in the SOC than the cathode, as between an SOC of 0 and 30% the anode layer can expand almost 10% and the Young's modulus can increase by 20% [67]. The Young's modulus of the anode triples as it becomes fully lithiated to LiC_6 [68]. The anode undergoes greater expansion during lithiation, seeing a volumetric expansion of 9.8% when charged from 0% to 30% SOC [67]. This is demonstrated across all peaks in Figure 6, where the TOF when fully charged (lithiated anode) is always less than when fully discharged (de-lithiated anode), i.e. the red dots are higher than the green dots in Figure 6. The volumetric expansion affects the TOF by affecting the propagation path of the acoustic signal; an increase in volume results in a longer path, and therefore the signal requires more time to cover the distance. This amplifies the change in TOF when combined with the change in the speed of sound, due to material properties. In the case of the permanent TOF shift, the continued growth in the SEI layer driving the LLI will gradually affect the TOF.

A shift to a shorter permanent TOF means the speed of sound has increased through the cell, whilst a shift to a longer TOF represents a decrease in the cell's speed of sound. There are a number of factors that could have caused this: a change in E ; a change in ρ , or a combination. It should be noted

Given the change seen in Figure 5 and general trend for Figure 6 of a decrease in permanent TOF, a relation of LLI to a negative shift in permanent TOF is not unreasonable. The inconsistency between the polarity of the correlations is likely to be caused by complex behaviours of multiple layers during cycling, as at each interface the ultrasonic signal will split as defined in Equation 5. It is worthy of note that the polarity can vary within the same signal, as Short A and Long A were from the same sensor monitoring the same cell. Similar results have been found in the literature. Reference [22] found that the selected peak saw a permanent shift to a shorter TOF as the NMC cell aged, while reference [20] saw a permanent shift to a longer TOF in the selected peak as the LCO cell aged. [19] also saw a permanent shift to a longer TOF in an LCO cell, but within 60 cycles the permanent shift gradually decelerated until there was no noticeable change in the TOF between cycles. It should be noted that the frequencies and the TOF of the selected peaks differed between these articles. However, all tracked peaks were from the first reflection. [20] noted that the TOF shift was likely due to swelling, while [22] and [19] did not discuss the degradation method.

Swelling was not detected within Cell A or Cell B. For Cell A, all short peaks (peaks within the first and second reflection) saw a permanent shift to a longer TOF, whilst all long peaks saw a permanent shift to a shorter TOF. This was not present in cell B, as the polarity matched between the two peaks. The direction of the permanent shifts seen in the cells matches that of that seen in [22], which had the same cell chemistry of NMC, whilst the others used a different cell chemistry. This suggests that the cell chemistry affects the direction of the permanent shift, though this would require further investigation.

3.4. State-of-health and ultrasonic fluctuations

As shown in Figure 4, the SOH measured in both cells underwent fluctuations as they degraded, particularly with cell B. Figures 8a and 8b show the SOH drop of cell A, with the Short A and Long A plotted alongside. The same for cell B can be seen in Figures 8b and 8d. There is a visible relationship between the SOH and TOF fluctuations.

Cell A experienced lower magnitude fluctuations than cell B; however, there was a significant drop around cycle 80, which is indicated by the black box. This perturbation is also observed in the ToF signal, despite the permanent shift leading to a longer TOF. The change in TOF was $0.167 \mu\text{s}$, which is $\sim 19\%$ of the total TOF shift. In comparison, the capacity fade of this perturbation was $\sim 15\%$ of the total capacity drop. There are also SOH peaks and valleys that are reflected in the TOF, namely around cycles 40 and 90. The fluctuations show a clear correlation with the TOF response, show in Figure 8. The fluctuations in Long A were greater in magnitude compared to the overall shift, along with a less linear shift as the cell was cycled. At cycle 80, the same significant valley is reflected; however, the

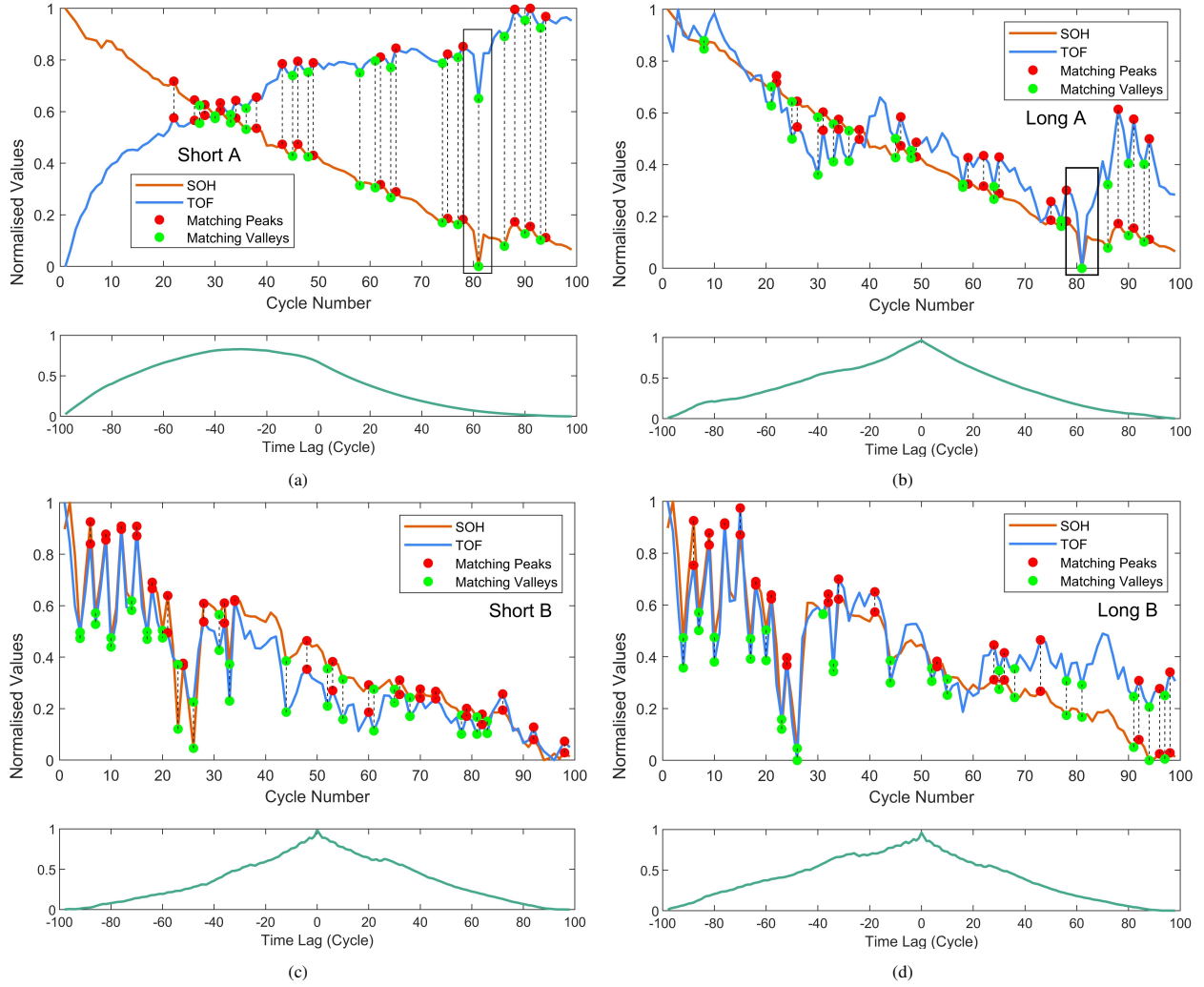


Figure 8: Matching peaks and valleys between the SOH estimation and TOF of Short A (a), Long A (b), Short B (c) and Long B (d). The time lag for the four peaks are also presented to highlight the sensitivity of the TOF to SOH changes.

amplitude of the TOF shift is more significant than in Short A. The change in TOF was $0.036\mu\text{s}$, which is $\sim 36\%$ of the total permanent shift. Both the short and long signals observed this shift. Cell B showed unstable SOH readings for the first 30 cycles, as shown by the significant fluctuations. Both the long and short TOF readings reflected these fluctuations as the signals oscillated in a similar manner.

Temporal dependencies between the time-of-flight (TOF) and state-of-health (SOH) were explored using the cross-correlation technique, implemented through MATLAB's 'xcorr' function. The introduced time lag (τ_{lag}) quantifies the temporal relationship, indicating the extent to which the TOF lags behind or leads the SOH. A positive τ_{lag} indicates that the TOF precedes the SOH, while a negative τ_{lag} suggests the reverse, with a τ_{lag} of 0 denoting a simultaneous change in the TOF and SOH. It can be seen in Figures 8b, 8c and 8d that τ_{lag} is 0 when the correlation coefficient

is highest. This alignment at $\tau_{\text{lag}} = 0$ indicates that the TOF dynamically shifts simultaneously with the SOH. In particular, the correlation strength is consistently observed to have its maximum value – all above 0.95 – at $\tau_{\text{lag}} = 0$ in the three subfigures. This is summarised in Table 3.

Peak	τ_{lag} (Cycle)	τ_{lag} Strength
Short A	-30	0.829
Long A	0	0.962
Short B	0	0.984
Long B	0	0.961

Table 3: Time lag location and strength for each peak.

For Figure 8a, the correlation for Short A is greatest at $\tau_{\text{lag}} = -30$ cycles with a range of lags at which the two signals have similarities. This suggests the SOH precedes the TOF by a range of possible cycles, where the strongest correlation occurring with a difference of 30 cycles. This is unlikely given the results from the other peak, notably the valley at cycle 81 matching with no delay. This behaviour is not seen in the other peaks, suggesting that the signal is exhibiting anomalous behaviour. This could be based on the direction of the TOF shift, as Short A is the only peak that underwent an increase in TOF as the cell capacity dropped.

4. Conclusion

Accurate estimation of cell state-of-health can contribute to the increase in the safety and longevity of lithium-ion cell utilisation. In this work, two cells with a cycle life of 301 cycles were cycled at a C-rate of 0.3C for 100 cycles within manufacturer capacity limits to induce non-abusive degradation. The results displayed a strong correlation between the change in the ultrasonic time-of-flight response and cell degradation when analysing longer reflections. The direction of the shift matches work using the same cell chemistry, while cells with different chemistries tested within literature were found to have a different direction in the permanent TOF shift.

For shorter reflections, they were observed to behave differently, with one cell showing a decreased permanent shift and the other an increased permanent shift. There are several reasons this may have occurred: one of them is manufacturing differences between the cells; another could be due to the transducer, as the Long TOF and Short TOF differed within the same signal. All reflections after Short A saw an increased permanent shift, the same as seen in cell B. Systematic testing showcased the feasibility of ultrasound in monitoring the state-of-health of lithium ion cells. Through the use of IC analysis, the primary degradation method for the cells was observed to be the loss of lithium-ion inventory.

The investigations also found that although the rate of degradation was linear, there were fluctuations observed, resulting in inconsistent loss in state-of-health estimates. Ultrasonic time-of-flight responses were identified to react

to these fluctuations, resulting in the detection of state-of-health variations that provide immediate responses. This was true regardless of the permanent shift direction. This offers the potential to observe regeneration phenomena and irregularities in the available capacity during operation. SOH anomalies can therefore be detected using ultrasound. However, a large dataset will be necessary for acoustic anomaly detection to be used on a larger scale.

In order to develop this dataset, standard and anomalous SOH fade would need to be accounted for. Controlling the variables that lead to SOH fade would be necessary to ensure the accuracy of the estimations. One such set of variables would be the various degradation methods. Inducing different degradation methods as the primary mechanism in similar cycling conditions could provide insight into the relation between capacity drop and the resultant ultrasonic response. This could be performed by repeating the tests at various C-rates and varying temperatures, or under- and over-charging the cells. Long cycling would allow for observations of degradation and ultrasonic behaviour as the cell reaches the end of life. Including post-mortem analysis could determine the sources of degradation and allow validation of the ultrasonic response. Investigating the effect of the cathode chemistry on the direction of the permanent shift could improve the viability of this method for SOH estimation, as this is in contention in literature. This can be done using simultaneous testing of multiple cells of differing cathode chemistries.

CRedit author statement

Daniel Williams: Conceptualisation, Data Curation, Formal Analysis, Investigation, Methodology, Writing - Original Draft, Visualisation, Writing - Review & Editing. **Joshua Green:** Investigation, Formal Analysis & Writing - Original Draft. **Peter Bugryniec:** Writing - Review and & Editing **Solomon Brown:** Supervision, Writing - Review & Editing. **Rob Dwyer-Joyce:** Conceptualisation, Supervision, Writing - Review & Editing.

Funding

The authors would like to acknowledge the financial support of the Faraday Institution BESAFE project FIRG038, Engineering and Physical Sciences Research Council Tribo-Acoustic Sensors EP/N016483/1, Centre for Doctoral Training in Integrated Tribology EP/L01629X/1, and the Centre for Doctoral Training in Energy Storage and its Applications EP/L016818/1.

Data availability

Will be made available upon request.

Declaration of competing interest

The authors declare that they have no known competing financial interests or personal relationships that could have appeared to influence the work reported in this paper.

References

- [1] B. Nykvist, M. Nilsson, Rapidly falling costs of battery packs for electric vehicles, *Nature Climate Change* 5 (2015). doi:10.1038/nclimate2564.
- [2] Y. Ding, Z. P. Cano, A. Yu, J. Lu, Z. Chen, Automotive li-ion batteries: Current status and future perspectives, *Nature Climate Electrochemical Energy Reviews* 2 (2019). doi:10.1007/s41918-018-0022-z.
- [3] T. A. Faunce, J. Prest, D. Su, S. Hearne, F. Iacopi, On-grid batteries for large-scale energy storage: Challenges and opportunities for policy and technology, *MRS Energy and Sustainability* 5 (10) (2018). doi:10.1557/mre.2018.11.
- [4] V. Ramadesigan, P. Northrop, S. De, S. Santhanagopalan, R. Braatz, V. Subramanian, Modeling and simulation of lithium-ion batteries from a systems engineering perspective, *Journal of the Electrochemical Society* 159 (2012). doi:10.1149/2.018203jes.
- [5] R. Copley, D. Cumming, Y. Wu, R. Dwyer-Joyce, Measurements and modelling of the response of an ultrasonic pulse to a lithium-ion battery as a precursor for state of charge estimation, *Journal of Energy Storage* 36 (2021). doi:10.1016/j.est.2021.102406.
- [6] G. Sahinoglu, M. Pajovic, Z. Sahinoglu, Y. Wang, P. Orlik, T. Wada, Battery state-of-charge estimation based on regular/recurrent gaussian process regression, *IEEE Transactions on Industrial Electronics* 65 (2018). doi:10.1109/TIE.2017.2764869.
- [7] D. How, M. Hannan, M. Lipu, P. Ker, State of charge estimation for lithium-ion batteries using model-based and data-driven methods: A review, *IEEE Access* 7 (2019). doi:10.1109/ACCESS.2019.2942213.
- [8] Y. Wang, J. Tian, Z. Sun, L. Wang, R. Xu, M. Li, Z. Chen, A comprehensive review of battery modeling and state estimation approaches for advanced battery management systems, *Renewable and Sustainable Energy Reviews* 131 (1) (2020). doi:10.1016/j.rser.2020.110015.
- [9] M. Bercibar, I. Gandiaga, I. Villareal, N. Omar, J. V. Mierlo, P. V. den Bossche, Critical review of state of health estimation methods of li-ion batteries for real applications, *Renewable and Sustainable Energy Reviews* 56 (2016). doi:10.1016/j.rser.2015.11.042.
- [10] D. Williams, R. Copley, P. Bugryniec, R. Dwyer-Joyce, S. Brown, A review of ultrasonic monitoring: Assessing current approaches to li-ion battery monitoring and their relevance to thermal runaway, *Journal of Power Sources* 590 (2024). doi:10.1016/j.jpowsour.2023.233777.
- [11] G. Plett, Extended kalman filtering for battery management systems of lipb-based hev battery packs: Part 1. background, *Journal of Power Sources* 134 (2004). doi:10.1016/j.jpowsour.2004.02.031.
- [12] I. Kim, A technique for estimating the state of health of lithium batteries through a dual-sliding-mode observer, *IEEE Transactions on Power Electronics* 25 (2010). doi:10.1109/TPEL.2009.2034966.
- [13] R. Xiong, L. Li, J. Tian, Towards a smarter battery management system: A critical review on battery state of health monitoring methods, *Journal of Power Sources* 405 (2018). doi:10.1016/j.jpowsour.2018.10.019.
- [14] G. Vennan, A. Sahoo, S. Ahmed, A survey on lithium-ion battery internal and external degradation modeling and state of health estimation, *Journal of Energy Storage* 52 (2022). doi:10.1016/j.est.2022.104720.
- [15] Y. Liu, C. Liu, Y. Liu, F. Sun, J. Qiao, T. Xu, Review on degradation mechanism and health state estimation methods of lithium-ion batteries, *Journal of Traffic and Transportation Engineering (English Edition)* 10 (2023). doi:10.1016/j.jtte.2023.06.001.
- [16] C. Weng, J. Sun, H. Peng, A unified open-circuit-voltage model of lithium-ion batteries for state-of-charge estimation and state-of-health monitoring, *Journal of Power Sources* 258 (2014). doi:10.1016/j.jpowsour.2014.02.026.
- [17] J. Remmlinger, M. Buchholz, T. Soczka-Guth, K. Dietmayer, On-board state-of-health monitoring of lithium-ion batteries using linear parameter-varying models, *Journal of Power Sources* 239 (2013). doi:10.1016/j.jpowsour.2012.11.102.
- [18] J. B. Robinson, M. Maier, G. Alster, T. Compton, D. Brett, P. Shearing, Spatially resolved ultrasound diagnostics of li-ion battery electrodes, *Physical Chemistry Chemical Physics* 21 (12) (2019). doi:10.1039/c8cp07098a.

- [19] G. Davies, K. Knehr, B. van Tassell, T. Hodson, S. Biswas, A. Hsieh, D. Steingart, State of charge and state of health estimation using electrochemical acoustic time of flight analysis, *Journal of The Electrochemical Society* 164 (12) (2017). doi:10.1149/2.1411712jes.
- [20] Y. Wu, Y. Wang, W. Yung, M. Pecht, Ultrasonic health monitoring of lithium-ion batteries, *Electronics* 8 (7) (2019). doi:10.3390/electronics8070751.
- [21] H. Popp, M. Koller, S. Keller, G. Glanz, R. Klambauer, A. Bergmann, State estimation approach of lithium-ion batteries by simplified ultrasonic time-of-flight measurement, *IEEE Access* 7 (2019). doi:10.1109/access.2019.2955556.
- [22] P. Ladpli, R. Nardari, F. Kopsaftopoulos, Y. Wang, F. Chang, Design of multifunctional structural batteries with health monitoring capabilities, *European Workshop on Structural Health Monitoring* (2016).
- [23] J. Krätzkramer, H. Krätzkramer, *Ultrasonic Testing of Materials*, 3rd Edition, Springer, 2013. doi:10.1007/978-3-662-02357-0.
- [24] F. Jiang, Y. Chen, S. Ju, Q. Zhu, L. Zhang, J. Peng, X. Wang, J. D. Miller, Ultrasound-assisted leaching of cobalt and lithium from spent lithium-ion batteries, *Ultrasonics Sonochemistry* 48 (2018). doi:https://doi.org/10.1016/j.ultsonch.2018.05.019.
- [25] C. Lei, I. Aldous, J. M. Hartley, D. L. Thompson, S. Scott, R. Hanson, P. A. Anderson, E. Kendrick, R. Sommerville, K. S. Ryder, A. P. Abbott, Lithium ion battery recycling using high-intensity ultrasonication, *Green Chemistry* 23 (2021). doi:10.1039/d1gc01623g.
- [26] S. Jie, J. Kang, S. Baek, B. Lee, Enhanced electrochemical performance of li-ion battery via ultrasonic-assisted inorganic-rich and thin sei layer, *Ultrasonics Sonochemistry* 100 (2023). doi:https://doi.org/10.1016/j.ultsonch.2023.106620.
- [27] V.-K. Wong, Y. Hu, Z. W. Tham, Y. F. Chen, M. Liu, K. E. Lim, S. J. Park, F. Cui, L. Zhang, Measurement of elastic constant matrix of carbon fiber composites with an ultrasonic 2d-array transducer, *IEEE Sensors Journal* 22 (2022). doi:10.1109/JSEN.2022.3149241.
- [28] B. Sun, C. Zhang, S. Liu, Z. Xu, L. Li, Ultrasonic inspection of pouch-type lithium-ion batteries: a review, *Nondestructive Testing and Evaluation* (2024). doi:10.1080/10589759.2024.2317866.
- [29] G. Zhao, Y. Liu, G. Liu, S. Jiang, W. Hao, State-of-charge and state-of-health estimation for lithium-ion battery using the direct wave signals of guided wave, *Journal of Energy Storage* 39 (2021). doi:10.1016/j.est.2021.102657.
- [30] J. Kim, J. Jo, J. Byeon, Ultrasonic monitoring performance degradation of lithium ion battery, *Microelectronics Reliability* 114 (200). doi:10.1016/j.microrel.2020.113859.
- [31] T. Guan, S. Sun, F. Yu, Y. Gao, P. Fan, P. Zuo, C. Du, G. Yin, The degradation of LiCoO₂/graphite batteries at different rates, *Electrochimica Acta* 279 (2018). doi:10.1016/j.electacta.2018.04.197.
- [32] R. Xiong, Y. Pan, W. Shen, H. Li, F. Sun, Lithium-ion battery aging mechanisms and diagnosis method for automotive applications: Recent advances and perspectives, *Renewable and Sustainable Energy Reviews* 131 (2020). doi:10.1016/j.rser.2020.110048.
- [33] T. Guan, S. Sun, Y. Gao, C. Du, P. Zuo, Y. Cui, L. Zhang, G. Yin, The effect of elevated temperature on the accelerated aging of LiCoO₂/mesocarbon microbeads batteries, *Applied Energy* 177 (2016). doi:10.1016/j.apenergy.2016.05.101.
- [34] D. Wong, B. Shrestha, D. Wetz, J. Heinzel, Impact of high rate discharge on the aging of lithium nickel cobalt aluminum oxide batteries, *Journal of Power Sources* 280 (2015). doi:10.1016/j.jpowsour.2015.01.110.
- [35] A. G. Hsieh, S. Bhadra, B. J. Hertzberg, P. J. Gjeltema, A. Goy, J. W. Fleischer, D. A. Steingart, Electrochemical-acoustic time of flight: in operando correlation of physical dynamics with battery charge and health, *Energy & Environmental Science* 8 (5) (2015). doi:10.1039/c5ee00111k.
- [36] H. Sun, N. Muralidharan, R. Amin, V. Rathod, P. Ramuhalli, I. Belharouak, Ultrasonic nondestructive diagnosis of lithium-ion batteries with multiple frequencies, *Journal of Power Sources* 549 (2022). doi:https://doi.org/10.1016/j.jpowsour.2022.232091.
- [37] S. Drake, M. Martin, D. Wetz, J. Ostanek, S. Miller, J. Heinzel, A. Jain, Heat generation rate measurement in a li-ion cell at large c-rates through temperature and heat flux measurements, *Journal of Power Sources* 285 (2015). doi:https://doi.org/10.1016/j.jpowsour.2015.03.008.

- [38] L. Spithoff, P. Shearing, O. Burheim, Temperature, ageing and thermal management of lithium-ion batteries, *Energies* 14 (2021). doi:10.3390/en14051248.
- [39] H. Amiri, B. Makkiabadi, A review of ultrasound thermometry techniques, *Frontiers in Biomedical Technologies* 7 (2020). doi:10.18502/fbt.v7i2.3852.
- [40] R. Copley, R. Dwyer-Joyce, Prediction of the internal structure of a lithium-ion battery using a single ultrasound wave response, *Journal of Energy Storage* 72 (2023). doi:10.1016/j.est.2023.108778.
- [41] S. P. B. Saha, K. Goebel, J. Christophersen, Prognostics methods for battery health monitoring using a bayesian framework, *IEEE Transactions on Instrumentation and Measurement* 58 (2009). doi:10.1109/TIM.2008.2005965.
- [42] B. Olivares, M. C. Muñoz, Particle-filtering-based prognosis framework for energy storage devices with a statistical characterization of state-of-health regeneration phenomena, *IEEE Transactions on Instrumentation and Measurement* 62 (2013). doi:10.1109/TIM.2012.2215142.
- [43] Z. Chen, Q. Xue, R. Xiao, Y. Liu, J. Shen, State of health estimation for lithium-ion batteries based on fusion of autoregressive moving average model and elman neural network, *IEEE Access* 7 (2019). doi:10.1109/ACCESS.2019.2930680.
- [44] D. Shin, M. Poncino, E. Macii, N. Chang, A statistical model-based cell-to-cell variability management of li-ion battery pack, *IEEE Transactions on Computer-Aided Design of Integrated Circuits and Systems* 34 (2) (2015). doi:10.1109/TCAD.2014.2384506.
- [45] M. Dubarry, N. Vuillaume, B. Y. Liaw, Origins and accommodation of cell variations in li-ion battery pack modeling, *International Journal of Energy Research* 34 (2) (2010).
- [46] G. Liu, M. Ouyang, L. Lu, J. Li, X. Han, Analysis of the heat generation of lithium-ion battery during charging and discharging considering different influencing factors, *Journal of Thermal Analysis and Calorimetry* 116 (2014). doi:10.1007/s10973-013-3599-9.
- [47] L. Zhang, L. Wang, C. Lyu, J. Li, J. Zheng, Non-destructive analysis of degradation mechanisms in cycle-aged Graphite/LiCoO₂ batteries, *Energies* 7 (2014). doi:10.3390/en7106282.
- [48] F. Soto, A. Marzouk, F. El-Mellouhi, P. Balbuena, Understanding ionic diffusion through sei components for lithium-ion and sodium-ion batteries: Insights from first-principles calculations, *Chemistry of Materials* 30 (2018). doi:10.1021/acs.chemmater.8b00635.
- [49] L. Yao, S. Xu, A. Tang, F. Zhou, J. Hou, Y. Xiao, Z. Fu, A review of lithium-ion battery state of health estimation and prediction methods, *World Electric Vehicle Journal* 12 (2021). doi:10.3390/wevj12030113.
- [50] D. Stroe, M. Swierczynski, S. Kær, R. Teodorescu, Degradation behavior of lithium-ion batteries during calendar ageing—the case of the internal resistance increase, *IEEE Transactions on Power Electronics* 54 (2018). doi:10.1109/TIA.2017.2756026.
- [51] H. Sun, J. Sun, K. Zhao, L. Wang, K. Wang, Data-driven ICA-Bi-LSTM-combined lithium battery soh estimation, *Mathematical Problems in Engineering* 2022 (2022). doi:10.1155/2022/9645892.
- [52] T. Pathan, M. Rashid, M. Walker, W. Widanage, E. Kendrick, Active formation of li-ion batteries and its effect on cycle life, *Journal of Physics: Energy* 1 (2019). doi:10.1088/2515-7655/ab2e92.
- [53] T. Plattard, N. Barnel, L. Assaud, S. Franger, J. Duffault, Combining a fatigue model and an incremental capacity analysis on a commercial nmc/graphite cell under constant current cycling with and without calendar aging, *Batteries* 5 (2019). doi:10.3390/batteries5010036.
- [54] M. Dubarry, D. Anseán, Best practices for incremental capacity analysis, *Frontiers in Energy Research* 10, This work is licensed under a Creative Commons Attribution 4.0 International License (CC BY 4.0) (2022). doi:10.3389/fenrg.2022.1023555.
- [55] I. Bloom, L. Walker, J. Basco, D. Abraham, J. Christophersen, C. Ho, Differential voltage analyses of high-power lithium-ion cells. 4. cells containing NMC, *Journal of Power Sources* 195 (2010). doi:10.1016/j.jpowsour.2009.08.019.
- [56] R. Carter, T. Kingston, R. Atkinson, M. Parmananda, M. Dubarry, C. Fear, P. Mukherjee, C. Love, Directionality of thermal gradients in

- lithium-ion batteries dictates diverging degradation modes, *Cell Reports Physical Science* 2 (2021). doi:10.1016/j.xcrp.2021.100351.
- [57] M. Kemeny, P. Ondrejka, M. Mikolasek, Incremental capacity analysis for prediction of li-ion battery degradation mechanisms: Simulation study, in: *The 13th International Conference on Advanced Semiconductor Devices And Microsystems*, 2020.
- [58] P. Ladpli, F. Kopsaftopoulos, F. Chang, Estimating state of charge and health of lithium-ion batteries with guided waves using built-in piezoelectric sensors/actuators, *Journal of Power Sources* (2018). doi:10.1016/j.jpowsour.2018.02.056.
- [59] J. Wang, J. Purewal, P. Liu, J. Hicks-Garner, S. Soukazian, W. Sherman, A. Sorenson, L. Vu, H. Tataria, M. Verbrugge, Degradation of lithium ion batteries employing graphite negatives and nickel-cobalt-manganese oxide p spinel manganese oxide positives: Part 1, aging mechanisms and life estimation, *Journal of Power Sources* 269 (2014). doi:10.1016/j.jpowsour.2014.07.030.
- [60] X. Han, M. Ouyang, L. Lu, J. Li, Y. Zheng, Z. Li, A comparative study of commercial lithium ion battery cycle life in electrical vehicle: Aging mechanism identification, *Journal of Power Sources* 251 (2014). doi:10.1016/j.jpowsour.2013.11.029.
- [61] R. Deshpande, M. Verbrugge, Y. Cheng, J. Wang, P. Liu, Battery cycle life prediction with coupled chemical degradation and fatigue mechanics, *Journal of The Electrochemical Society* 159 (2012). doi:10.1149/2.049210jes.
- [62] K. Meng, X. Chen, W. Zhang, W. Chang, J. Xu, A robust ultrasonic characterization methodology for lithium-ion batteries on frequency-domain damping analysis, *Journal of Power Sources* 547 (2022). doi:10.1016/j.jpowsour.2022.232003.
- [63] S. Santhanagopalan, R. E. White, Quantifying cell-to-cell variations in lithium ion batteries, *International Journal of Electrochemistry* 2012 (1) (2012). doi:10.1155/2012/395838.
- [64] J. O. Majasan, J. B. Robinson, R. E. Owen, M. Maier, A. N. P. Radhakrishnan, M. Pham, T. G. Tranter, Y. Zhang, P. R. Shearing, D. J. L. Brett, Recent advances in acoustic diagnostics for electrochemical power systems, *Journal of Physics* 3 (3) (2021). doi:10.1088/2515-7655/abfb4a.
- [65] Y. Preger, H. Barkholtz, A. Fresquez, D. Campbell, B. Juba, J. Romàn-Kustas, S. Ferreira, B. Chalamala, Degradation of commercial lithium-ion cells as a function of chemistry and cycling conditions, *Journal of The Electrochemical Society* 167 (2020). doi:10.1149/1945-7111/abae37.
- [66] Y. Li, M. Bettge, B. Polzin, Y. Zhu, M. Balasubramanian, D. P. Abraham, Understanding long-term cycling performance of $\text{Li}_{1.2}\text{Ni}_{0.15}\text{Mn}_{0.55}\text{Co}_{0.1}\text{O}_2$ -Graphite lithium-ion cells, *Journal of The Electrochemical Society* 160 (2013). doi:10.1149/2.002305jes.
- [67] J. Xu, B. Liu, D. Hu, State of charge dependent mechanical integrity behavior of 18650 lithium-ion batteries, *Scientific Reports* 6 (2016). doi:10.1038/srep21829.
- [68] Y. Qi, H. Guo, L. Hector, A. Timmons, Threefold increase in the young's modulus of graphite negative electrode during lithium intercalation, *Journal of the Electrochemical Society* 157 (2010). doi:10.1149/1.3327913.